Draft version February 19, 2025
Typeset using LaTeX **twocolumn** style in AASTeX631

arXiv:2410.06960v4 [astro-ph.GA] 18 Feb 2025

Blowing star formation away in AGN Hosts (BAH) - II. Investigating the origin of the H_2 emission excess in nearby galaxies with JWST MIRI

Rogemar A. Riffel [1], Gabriel L. Souza-Oliveira [1], José Henrique Costa-Souza [1], Nadia L. Zakamska [2], Thaisa Storchi-Bergmann [3], Rogério Riffel [3] and Marina Bianchin [4]

[1] *Departamento de Física, CCNE, Universidade Federal de Santa Maria, Av. Roraima 1000, 97105-900, Santa Maria, RS, Brazil*
[2] *Department of Physics & Astronomy, Johns Hopkins University, Bloomberg Center, 3400 N. Charles St, Baltimore, MD 21218, USA*
[3] *Departamento de Astronomia, IF, Universidade Federal do Rio Grande do Sul, CP 15051, 91501-970, Porto Alegre, RS, Brazil*
[4] *Department of Physics and Astronomy, 4129 Frederick Reines Hall, University of California, Irvine, CA 92697, USA*

ABSTRACT

We use James Webb Space Telescope (JWST) Mid-Infrared Instrument (MIRI) medium-resolution spectrometer (MRS) observations of 3C 293 (UGC 8782), CGCG 012-070 and NGC 3884 to investigate the origin of the H_2 emission. These three nearby Active Galactic Nucleus (AGN) hosts are known to present H_2 emission excess relative to star-forming galaxies, as traced by the H_2 S(3)/PAH$_{11.3\mu m}$ line ratio. We define the kinematically disturbed region (KDR) by the AGN and the virially dominated region (VDR) based on the H_2 line widths, using the $W80$ parameter. From the correlations between $W80$ and H_2 S(3)/PAH11.3μm, as well as the higher H2 S(5)/H2 S(3) and [Fe II]5.34 μm/PAH11.3μm ratios and flatter power-law temperature distributions observed in the KDR, we conclude that the H_2 emission in the KDR is primarily driven by shock-heated gas. For 3C 293, the KDR is co-spatial with the radio core, indicating that the origin of the shocks is the interaction of the radio jet with the interstellar medium, which is also responsible for the observed molecular and ionized gas outflows in this source. The other galaxies are weak radio sources; however, due to the lack of high-resolution radio images, we cannot rule out low-power jets as the origin of the shock-heated H_2. Our results indicate that the excess H_2 emission excess is associated to shock heating of the gas, generated by outflows or by the interaction of the radio jet with the ambient gas.

Keywords: galaxies: active – galaxies: ISM – galaxies: evolution – galaxies: kinematics and dynamics

1. INTRODUCTION

The molecular hydrogen (H_2) is the most abundant molecule in the Universe and the raw fuel of star formation (e.g. Omont 2007). However, the origin of H_2 emission and dynamics in extreme environments, such as active galactic nuclei (AGN), remains poorly understood. Atacama Large Millimeter Array (ALMA) observations have mapped the cold molecular gas ($T \lesssim$100 K) in nearby AGN hosts, uncovering signs of inflows and outflows (e.g. Alonso-Herrero et al. 2019). These studies use tracer molecules such as CO and HCN, without directly mapping H_2 emission or extending beyond the cold molecular phase. Ground-based near-infrared integral field unit (IFU) observations provide direct insights into the emission of the H_2 molecule (using the vibrational H_2 transitions, mostly in the K-band), but are confined to the hot molecular gas ($T \gtrsim$1000 K), which represents only a hot skin of the molecular gas content in the central region of nearby galaxies (Riffel et al. 2021b, 2023b). The physics and dynamics of warm molecular gas phase (100 K $\lesssim T \lesssim$ 1000 K) is now accessible through observations with the James Webb Space Telescope (JWST), which have the spatial and spectral resolutions necessary to resolve the emission structure and kinematics of ro-vibrational lines of H_2 in the mid-infrared (MIR).

Indirect evidence of the AGN's effect on the origin of H_2 MIR is provided through observations with the Spitzer telescope. Lambrides et al. (2019) conducted a compreheensive analysis on the spectra of a sample comprising 2015 galaxies observed with Spitzer's Infrared Spectrograph, encompassing both AGN hosts and star-forming galaxies. They derived the excitation temperatures of the H_2 and found that AGN-dominated galaxies exhibit temperatures, on average, 200 K higher than those without AGN, consistent with

previous results in smaller sub-samples (Petric et al. 2018). In addition, Lambrides et al. (2019) found that AGN hosts present an H_2 emission excess over what is expected for pure star formation, parameterized by the $H_2S(3)$ 9.665μm/PAH 11.3μm. Riffel et al. (2020b) conducted a follow-up study investigating the properties of optical emission lines by cross-correlating Lambrides et al. (2019) sample with the third-generation Sloan Digital Sky Survey (SDSS-III) database (Gunn et al. 2006; Eisenstein et al. 2011; Smee et al. 2013; Thomas et al. 2013). This comparison reveals a strong association between the H_2 emission excess and shock tracers in neutral gas, such as high values of [O I]λ6300 velocity dispersion and high [O I]λ6300/Hα line ratio (e.g. Allen et al. 2008; Ho et al. 2014; Dors et al. 2021). This indicates that galaxies with a high $H_2S(3)$ 9.665μm/PAH 11.3μm ratio may experience an excess of H_2 emission due to shocks resulting from the interaction of outflows with the ambient gas. This is further reinforced by simulations, which suggest that molecules could be generated within the outflow, exhibiting excitation properties indicative of shock heating (Richings & Faucher-Giguère 2018a,b).

The use of JWST, in combination with the Mid-Infrared Instrument (MIRI) medium-resolution spectrometer (MRS), enables detailed studies of the emission and dynamics of warm molecular gas in nearby galaxies, utilizing the MIR rotational H_2 lines. Results obtained with MIRI in the study of molecular gas in nearby galaxies include: increased emissions of warm and hot H_2 as well as ionized gas, which coincide with the intersection of the jet with dust lanes in the disk of NGC 7319 (Pereira-Santaella et al. 2022); regions of increased H_2 velocity dispersion between the nucleus and the star-forming ring in NGC 7469, attributed to shocks generated by ionized outflows (U et al. 2022); a wealth of interacting structures among various gas phases in the intergalactic medium in Stephan's Quintet, with strong MIR H_2 line emissions from warm gas generated by the fragmentation of dense cold molecular clouds, followed by mixing in the post-shock gas (Appleton et al. 2023); a collimated outflow of warm molecular gas originating from the southern nucleus of the ultra-luminous infrared galaxy NGC 3256, which is co-spatial with the outflow in cold gas observed by ALMA (Sakamoto et al. 2014). The warm to cold mass fraction is roughly 4%; a large fraction of warm molecular gas, accounting for 75% of the total molecular gas mass, in M83 (Hernandez et al. 2023); powerful jet-driven outflows in warm molecular gas in the inner few kpc of nearby ($z < 0.1$) radio-loud AGN (Leftley et al. 2024; Costa-Souza et al. 2024); evidence of shock excitation of H_2 and detection of warm molecular outflows within the ionization cones of the nearby Seyfert galaxy NGC 5728 (Davies et al. 2024). Ogle et al. (2025) used MIRI, along with near-infrared and optical integral field spectroscopy, to study Cygnus A, revealing a density-stratified NLR shaped by the interaction of the radio jet with the interstellar medium, and multi-phase biconical outflows reaching velocities of 600–2000 km s^{-1}.

Here, we use JWST MIRI MRS to investigate the origin of the H_2 emission excess in three nearby active galaxies: 3C 293, CGCG 012-070 and NGC 3884. These targets were selected from Riffel et al. (2020b), identified as the most extreme objects in terms of $H_2S(3)$ 9.665μm/PAH 11.3μm, [O I]λ6300 velocity dispersion and high [O I]λ6300/Hα line ratio, indicating they may be potential hosts of molecular gas outflows and shocks. This paper is structured as follows: Section 2 introduces the targets and the data, Sec. 3 presents our results, which are discussed in Sec. 4. Finally, our main conclusions are summarized in Sec. 5.

2. TARGETS AND DATA

2.1. *The galaxies*

3C 293 (UGC 8782) presents a complex optical morphology, leading to its classification both as a spiral galaxy (e.g. Sandage 1966; de Vaucouleurs et al. 1991) and as a dusty elliptical (e.g. Ebneter & Balick 1985; Tremblay et al. 2007). It is located at a redshift $z = 0.045$ (Sandage 1966), is host of a Low-Ionization Nuclear Emission Region (LINER; Véron-Cetty & Véron 2006) and is a radio loud source classified as Fanaroff-Riley (FR) II (Fanaroff & Riley 1974; Liu & Zhang 2002), displaying a double-double radio structure. The inner radio lobes are observed at scales of ∼4 kpc, aligned along the east-west direction, while the outer lobes span approximately 200 kpc along the northwest-southeast direction (e.g., Machalski et al. 2016). Subarcsecond radio imaging of the 3C 293 indicates it has gone through multiple activity epochs, with a compact young nuclear steep spectrum (CSS) source, and it is classified as a jet with short interruption time periods (Kukreti et al. 2022).

In the optical, 3C 293 presents dust filaments spanning scales from 10^2–10^3 pc, which have been interpreted as a result of a previous merger event (e.g. Martel et al. 1999). Outflows co-spatial with the inner radio jet have been observed in ionized gas (Emonts et al. 2005; Mahony et al. 2016; Riffel et al. 2023a) with velocities of ∼1000 km s^{-1}, and in neutral hydrogen (Morganti et al. 2003) with velocities of up to 1400 km s^{-1}. The ionized gas emission in the inner 2 kpc of this galaxy is primarily attributed to photoionization by the central

AGN, with an additional contribution from shocks for the outflow component, due to the interaction of the radio jet with the surrounding gas (Riffel et al. 2023a). Previous Spitzer observations of 3C 293 reveal strong jet-shocked H_2 emission (Ogle et al. 2010), indicating that the radio jet drives both the outflow and the heating of the warm H_2 gas (Guillard et al. 2012). While the outflows are not detected in cold molecular gas (Labiano et al. 2014), Costa-Souza et al. (2024) report the detection of outflows in warm H_2, using JWST MIRI MRS data. The warm molecular outflows are observed cospatial with the radio core and these authors estimated a mass-outflow rate of $\approx 6\,M_\odot\,yr^{-1}$, which is one order of magnitude larger than the ionized gas outflows rate. If sustained, these outflows are capable of expelling all warm molecular gas from the central region of the galaxy in just 1 Myr (Costa-Souza et al. 2024).

CGCG 012-070 is a highly inclined Sb spiral galaxy, with axis ratio of $b/a \approx 0.3$ (Kautsch et al. 2006), located at a redshift $z = 0.048$ (e.g. Nair & Abraham 2010). Its nuclear nuclear activity is classified as a Seyfert 2 AGN (e.g. Véron-Cetty & Véron 2006). This galaxy presents faint radio emission, with a 1.4 GHz luminosity of $L_{1.4} \approx 2.4 \times 10^{22}$ W Hz^{-1} measured from the Faint Images of the Radio Sky at Twenty centimeters (FIRST) survey (Becker et al. 1995; Lofthouse et al. 2018; Lin et al. 2018). The nuclear optical spectrum CGCG 012-070 exhibits intense emission lines, which can be represented by two kinematic components, a broad base and a narrow component, suggesting the presence of an outflow in ionized gas (Gunn et al. 2006). This is further confirmed by IFU observations, which reveal that the broad component is associated with a nuclear outflow, while the narrow component refers to the emission from the gas in the disk (Ramos Vieira, priv. comm.).

NGC 3884 (UGC 6746) is the closest of the three galaxies, with a redshift of $z = 0.023$ (Rines et al. 2016, e.g.), classified as a Sab spiral (Tully & Pierce 2000). Its nuclear activity has been classified as a LINER with a faint Hα emission from the broad line region (Véron-Cetty & Véron 2006; Riffel et al. 2024). The ionized and neutral gas kinematics in the inner ~ 1.4 kpc of NGC 3884 present three kinematic components: a disc component similar to that observed for the stars; an inflowing gas component or gas externally acquired in previous merger events, observed as a twist in the kinematic position angle of the gas velocity field in the inner ~ 340 pc; an outflow detected as broad components to the emission lines ($\sigma \sim$250–400 km s^{-1}), with a maximum mass outflow rate of $0.25\pm0.15\ M_\odot\,yr^{-1}$ (Cazzoli et al. 2018; Hermosa Muñoz et al. 2022; Riffel et al. 2024). This galaxy presents a faint radio source with $L_{\rm FIRST} \approx 1.01 \times 10^{22}$ W Hz^{-1} (Lofthouse et al. 2018; Lin et al. 2018).

2.2. *The data and measurements*

We use MIR JWST spectroscopic data obtained with the Mid-Infrared Instrument medium-resolution spectrometer (MIRI MRS; Wells et al. 2015; Labiano et al. 2021; Argyriou et al. 2023a), as part of a Cycle 1 JWST proposal (Prop. ID: 1928, PI: Riffel, R. A.). We used a dither pattern consisting of four points, incorporating 30 groups with a single integration per dither position. Utilizing the slow readout mode, our total exposure time on the each source amounted to 1 hour and 35 minutes, plus 24 minutes of background exposure. For 3C 293 and CGCG 012-070, we used the sub-bands Short and Long, while for NGC 3884, the sub-bands Medium and Long were used. These sub-bands were selected to include at least the H_2 S(1) 17.03 μm and H_2 S(3) 9.665 μm emission lines in all galaxies, used to trace the warm molecular gas kinematics and essential to probe the gas temperature and masses. The observed spectral range also includes PAH features (at 11.3 and 6.2 μm), that can be used to map the H_2/PAH ratio, as well as emission lines from the ionized gas.

Here, we focus mainly in the 9.5–12 μm spectral region, which falls in the channel 2 Long sub-band, and use the H_2 S(3)/PAH$_{11.3\mu m}$ emission-line ratio to investigate the H_2 emission excess observed in these galaxies. The angular resolution of the datacubes is approximately 0.32 arcsec as given by the full width at half maximum (FWHM) of the JWST Point Spread Function (PSF), as measured from datacube for the star HD 2811. We incorporate to our analysis other H_2 rotational lines and the [Fe II]$_{5.34\,\mu m}$ which contribute to our understanding of the the H_2 excitation source. The data processing was conducted using the JWST Science Calibration Pipeline (Bushouse et al. 2024), version 1.13.4, along with the reference file `jwst_1188.pmap`. Additionally, optimized routines were employed for outlier detection and removal of artifacts. A detailed description of the observations and data reduction procedure is presented in Souza-Oliveira et al. (2024).

We employed the IFSCUBE Python package (Ruschel-Dutra et al. 2021) to fit the profiles of the strongest emission lines by Gauss-Hermite functions, in a continuum subtracted cube. The continuum subtraction was made by applying a double locally weighted scatterplot smoothing (lowess) for each spectral interval in the observed spectrum, using 30% and 10% of the data points in this order, followed by a linear interpolation. Although lowess smoothing does not properly constitute a

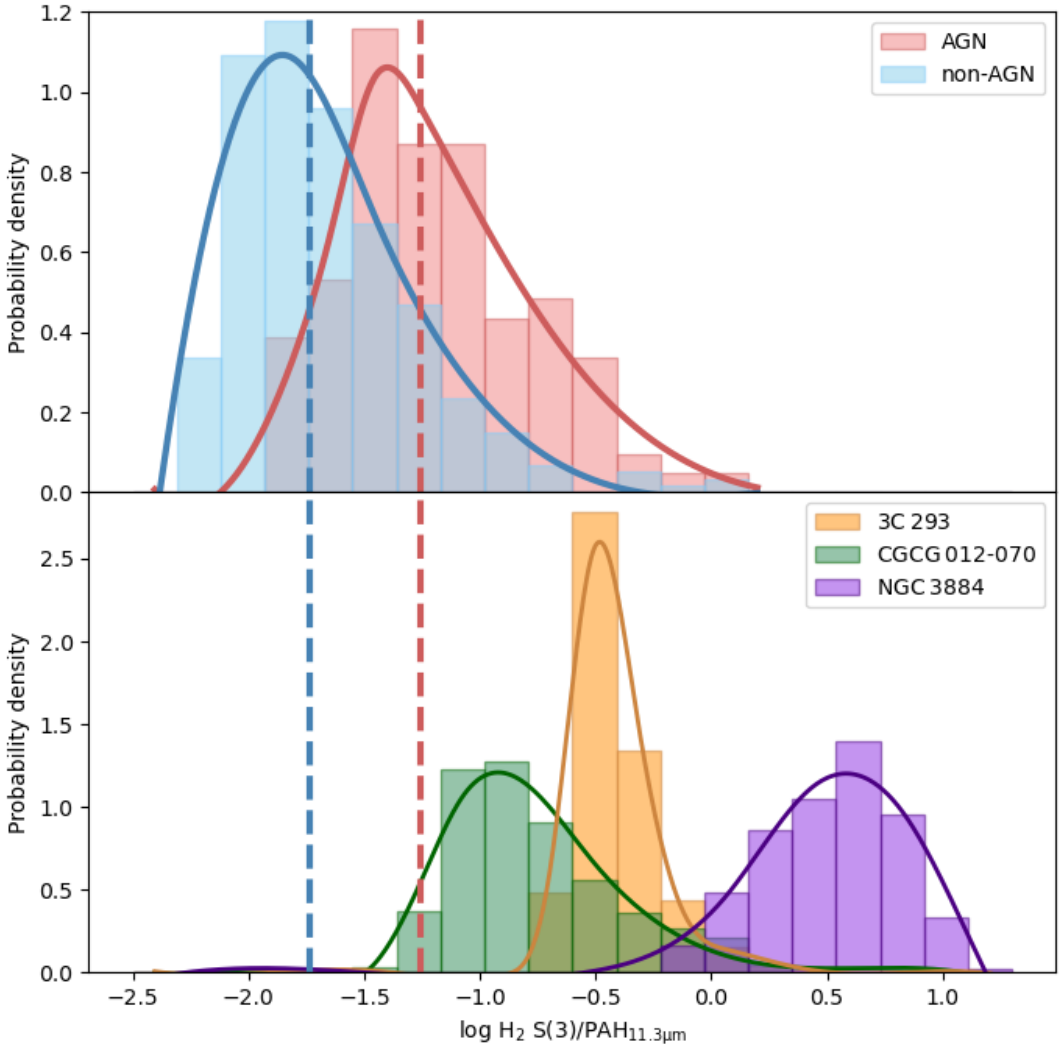

Figure 1. The top panel shows distributions of the H_2 S(3)/$PAH_{11.3\mu m}$ flux line ratios for AGN (light red) and non-AGN (light blue) hosts, based on the Spitzer data integrated over the entire galaxies, compiled by Lambrides et al. (2019). The bottom panel shows the distribution of the observed H_2 S(3)/$PAH_{11.3\mu m}$ flux line ratios per spaxel for CGCG 012-070 (green), 3C 293 (orange) and NGC 3884 (purple). The y-axis represents the probability density of values for each distribution, so that the integral of the area under the histogram equals 1. The solid lines show the smoothed distributions for each histogram, while the dashed vertical lines show the median values of H_2 S(3)/$PAH_{11.3\mu m}$ observed for AGN (red) and non-AGN (blue) hosts using the Spitzer dataset.

fitting method, it has shown to be effective and a simpler solution than polynomial fitting, given the complexity of the spectra and the resampling noise of spectral cubes. To initialize the emission line fitting process, we start by fitting the the nuclear spaxel. After successfully fitting the emission line profiles for the nucleus, these parameters serve as initial guesses for neighboring spaxels, following a spiral loop pattern. In the IFSCUBE code, we set the *refit* parameter to utilize the best-fit parameters from spaxels located within distances less than 0.3 arcsec as the starting point for subsequent fits.

The IFSCUBE code generates a data cube that contains the best-fit parameters. These parameters are then used to map the distributions of emission line flux and their kinematics. In addition, we use the IFSCUBE code to construct maps of the W_{80} parameter, corresponding to the width of the line profile containing 80 per cent of its total flux. Finally, $PAH_{11.3\mu m}$ flux maps are obtained by direct integration of the observed emission feature, after the subtraction of the underlying continuum. In all maps, we exclude regions where the emission line amplitude is lower than 3 times the standard deviation of the continuum in a nearby spectral range, free of emission lines.

3. RESULTS

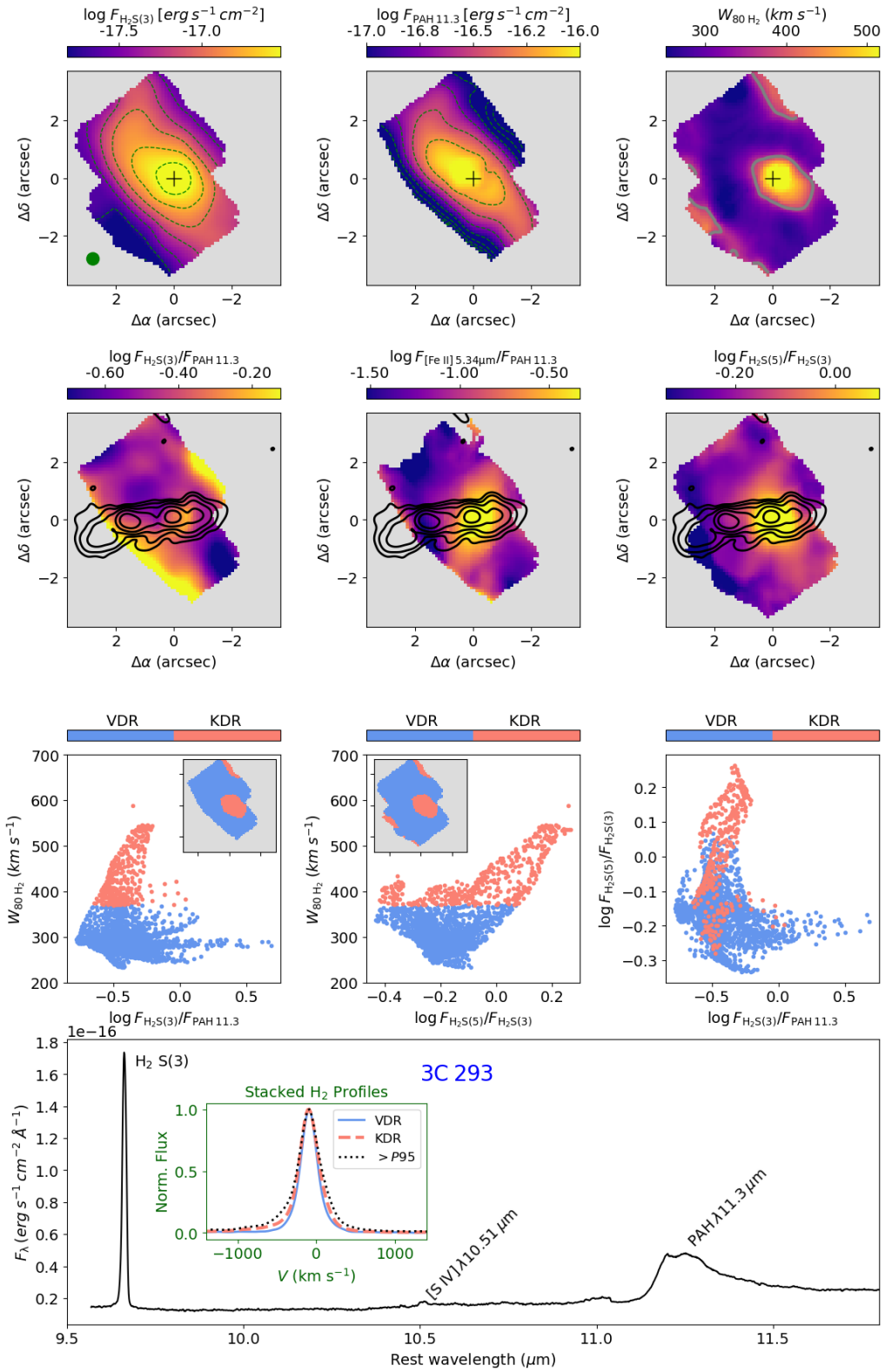

Figure 2. Results for 3C 293. The top panels show, from left to right, the H_2 S(3) and $PAH_{11.3\mu m}$ flux maps, and the W_{80} map for the H_2 S(3) emission line. The green filled circle shows the PSF FWHM and the dashed gray contours show flux levels from each image. The contours in the W_{80} map show the threshold used separate the virially dominated (VDR) and kinematically disturbed regions (KDR). The central plus signs represent the position of the peak of the continuum emission. The 2nd row shows the H_2 S(3)/$PAH_{11.3\mu m}$, [Fe II]$_{5.34\,\mu m}$/$PAH_{11.3\mu m}$ and H_2 S(5)/H_2 S(3) ratio maps. The contours are from the 1360 MHz radio image of 3C 293 from Kukreti et al. (2022). The 3rd row show plots of W_{80H_2} vs. log H_2 S(3)/$PAH_{11.3\mu m}$, W_{80H_2} vs. log H_2 S(5)/H_2 S(3) and log H_2 S(5)/H_2 S(3) vs. log H_2 S(3)/$PAH_{11.3\mu m}$. The insets indicate the KDR and VDR. The bottom panel shows a spectrum integrated within an aperture of 2.5 arcsec radius, covering the spectral region from 9.5 to 11.8 μm. The H_2 S(3), [S IV]λ10.51 μm and $PAH_{11.3\mu m}$ features are labeled. The inset shows stacked profiles for the H_2 S(3) emission line in the VDR and KDR. In all maps, the gray regions correspond to locations where the corresponding emission line is not detected above 3 σ of the continuum noise level or is not covered by the observed field of view.

Figure 1 presents the $\log H_2$ S(3)/PAH$_{11.3\mu m}$ emission-line ratio distributions for AGN (in red) and non-AGN (in blue) hosts as obtained from the Spitzer data, using the fluxes from Lambrides et al. (2019). In this plot, AGN are defined as those objects with 6.2 μm PAH equivalent width, EQW$_{6.2\,\mu m} < 0.27$ μm, while non-AGN have EQW$_{6.2\,\mu m} > 0.27$ μm (e.g. Stierwalt et al. 2013). The total number of AGN in the sample is 109, with a median value of $\log H_2$ S(3)/PAH$_{11.3\mu m} = -1.26$, while the median value for the 313 non-AGN sample is $\log H_2$ S(3)/PAH$_{11.3\mu m} = -1.74$. These values are indicated by the red and blue vertical dashed lines for AGN and non-AGN hosts, respectively. The bottom panels of Fig. 1 show the $\log H_2$ S(3)/PAH$_{11.3\mu m}$ distributions for 3C 293, CGCG 012-070 and NGC 3884, obtained with JWST. As can be observed, the three galaxies present higher values than the median one observed in the Spitzer AGN sample, with the highest ratios seen for NGC 3884.

In Figure 2, we present the results for 3C 293. The bottom panel shows an integrated spectrum in the 9.5–12 μm spectral region, within a circular aperture of 2.5 arcsec radius, centered at the galaxy nucleus, defined as the position corresponding to the peak of the continuum emission. This galaxy presents strong H_2 S(3) and PAH$_{11.3\mu m}$ features, with extended emission observed over the whole MIRI MRS field of view (FoV), as seen in the first two panels of the top row. The H_2 emission peak is observed at the galaxy nucleus and is more elongated along the northeast-southwest direction (orientation of the galaxy's major axis), revealing spiral arms to both sides of the nucleus. The PAH emission is also extended along the same direction, showing clearly the spiral arms. It can be noticed that the peak of the PAH emission is slightly displaced to the east of the position where H_2 emission peaks, which is co-spatial with the MIR emission center. The PAH emission peak is coincident with the location of the optical center of 3C 293. As already noticed in Riffel et al. (2023a) and Costa-Souza et al. (2024), the optical center of emission displaced about 0.6 arcsec from the MIR emission center, likely due to higher extinction in the optical continuum.

The top-right panel of Fig. 2 shows the W_{80} map for the H_2 S(3) emission line ($W_{80\,H_2}$) for 3C 293. The highest values of up to $\sim$500 km s^{-1} are observed surrounding the galaxy's nucleus, slightly extending to the west of it. Some high $W_{80\,H_2}$ values are also seen in regions close to the border of the MIRI MRS FoV, mainly to the northwest and east/southeast of the nucleus. The lowest values of $W_{80\,H_2} \approx 200$ km s^{-1} are observed surrounding the nucleus at distances of $\sim$1.5 arcsec from it and in regions along the spiral arms seen in the H_2 and PAH flux distributions. The $W_{80\,H_2}$ values presented here are not corrected by instrumental broadening ($\sigma_{ins} \approx$40 km s^{-1}; Argyriou et al. 2023b), which is negligible for the range of values observed.

The left panel in the second row of Fig. 2 shows the H_2 S(3)/PAH$_{11.3\mu m}$ line ratio map for 3C 293. The highest values of up to $\log H_2$/PAH$\approx$ 0 are observed at the nucleus and in regions farther away from it along the southeast-northwest direction. The lowest values of $\log H_2$ S(3)/PAH≈ -0.7 are seen mainly along the northeast-southwest direction, along the galaxy's disk major axis. For comparison, the middle panel of the second row shows the [Fe II]$_{5.34\,\mu m}$/PAH$_{11.3\mu m}$ line ratio map, which displays similar structures as those seen in the H_2 S(3)/PAH$_{11.3\mu m}$ ratio map. The [Fe II] emission is usually associated with shocks in partially ionized gas, that destroy dust grains releasing the iron into the gaseous phase (e.g. Storchi-Bergmann et al. 2009; Riffel et al. 2013, 2014; Hill & Zakamska 2014). The right panel of this row shows the $\log H_2$ S(5)/H_2 S(3) ratio map, a tracer of the gas temperature. The highest ratios (highest temperatures) are observed in regions co-spatial with locations where the highest H_2 S(3)/PAH$_{11.3\mu m}$ values are seen. It is evident that the highest values of the three ratios are observed in regions co-spatial with the radio core, as indicated by the black contours representing the 1360 MHz radio image of 3C 293 from Kukreti et al. (2022).

The third row of Fig. 2 show plots of $W_{80\,H_2}$ vs $\log H_2$ S(3)/PAH$_{11.3\mu m}$, $W_{80\,H_2}$ vs. $\log H_2$ S(5)/H_2 S(3) and $\log H_2$ S(5)/H_2 S(3) vs. $\log H_2$ S(3)/PAH$_{11.3\mu m}$, which will be further used to discuss the origin of the H_2 emission in the next section.

Figure 3 shows the results for CGCG 012-070. This galaxy displays strong H_2 and PAH emission, as revealed by the integrated spectrum shown in the bottom panel of Fig. 3. The relative intensity of the [S IV]10.51 μm emission line is larger, as compared to 3C 293. The H_2 emission is extended over the inner $\sim$1.8 arcsec, peaking at the nucleus and slightly more elongated to the northwest. The PAH emission is elongated along the southwest-northwest direction following the orientation of the galaxy's major axis. The highest PAH flux levels are observed at the north side of the nucleus and a "V-shaped" structure is observed close to the edge of the FoV to the southeast. The highest H_2 S(3)/PAH$_{11.3\mu m}$ values, of $\sim$1.25, are observed at the nucleus, decreasing with the distance from it. A similar behaviour is observed for the [Fe II]$_{5.34\,\mu m}$/PAH$_{11.3\mu m}$ line ratio map, with the largest values reaching [Fe II]$_{5.34\,\mu m}$/PAH$_{11.3\mu m} \approx 1.0$. The highest values of the H_2 S(5)/H_2 S(3) flux ra-

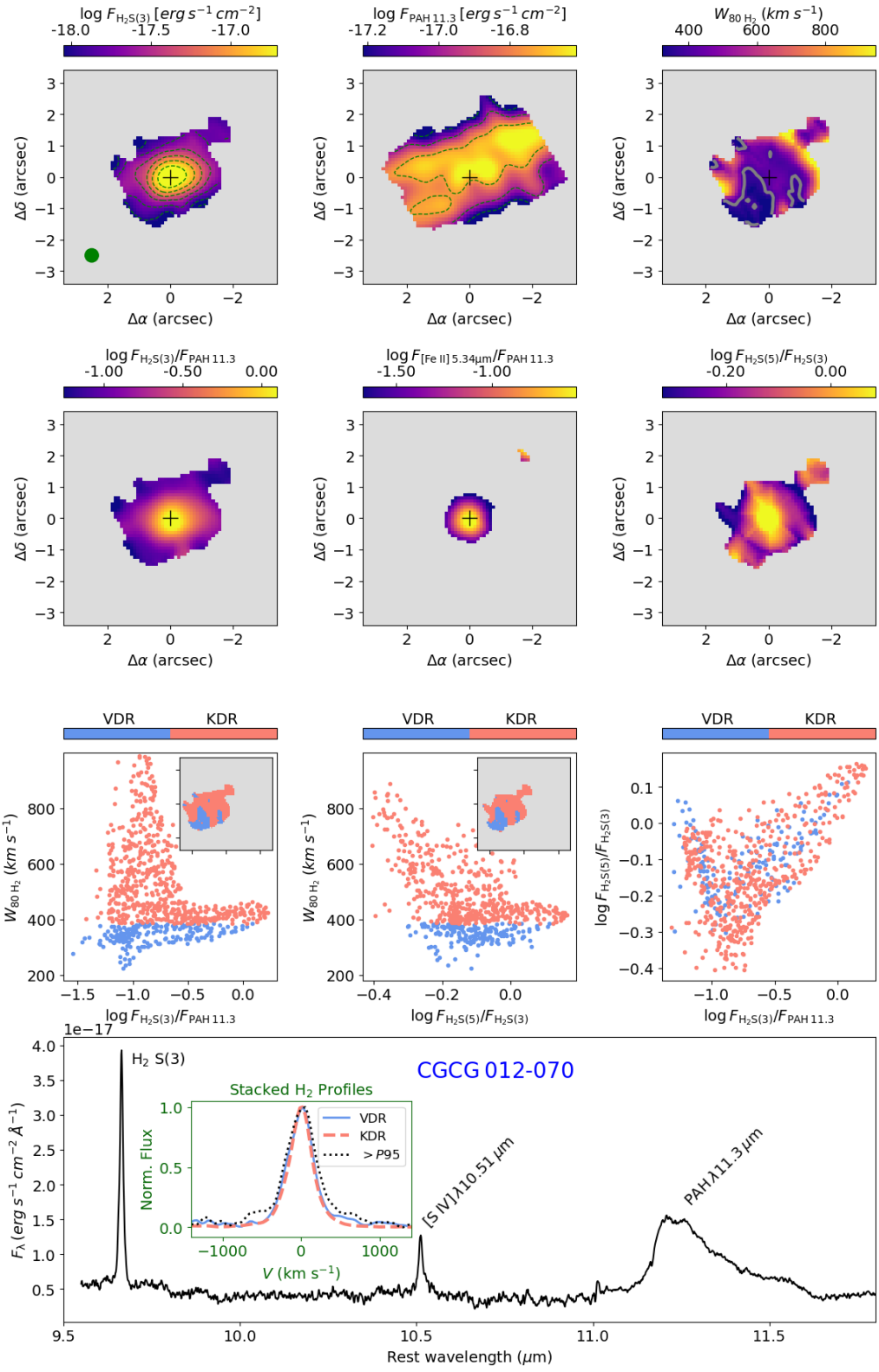

Figure 3. Same as Fig. 2, but for CGCG 012-070. Radio contours are not shown as there are no high resolution radio data available for this galaxy.

tio are concentrated in the innermost region and gradually decrease with increasing distance from the nucleus. The $W_{80\,H_2}$ map for this galaxy presents values of up to ∼900 km s^{-1}, mostly in regions away from the nucleus, but a linear structure of intermediate values (∼600 km s^{-1}) is also observed along the northeast-southwest direction, crossing the galaxy's nucleus.

The results for NGC 3884 are shown in Fig. 4. As this galaxy was observed in the MIRI MRS sub-bands Medium and Long, instead of Short and Long, as for the other two galaxies, its integrated spectrum does not include the region beyond 11.5 μm. But, the covered spectral range is still enough to include the PAH$_{11.3\mu m}$ feature at the galaxy's redshift. The H_2 emission in NGC 3884 is observed over the whole FoV, with the peak of emission seen at the nuclear position. On the other hand, the PAH$_{11.3\mu m}$ emission is detected only in a partial ring with inner and outer radii of ∼0.3 arcsec and 1.8 arcsec, respectively. This is the galaxy with the highest H_2 S(3)/PAH$_{11.3\mu m}$ among the three, with values of up to ∼10, much larger than the median values observed in AGN hosts observed by the Spitzer telescope (Fig. 1). The observed spectral range also does not include the [Fe II]$_{5.34\,\mu m}$ emission line. The H_2 S(5)/H_2 S(3) presents the highest values in the inner 0.5 arcsec from the nucleus in a structure elongated along the east west direction. The highest $W_{80\,H_2}$ values ($\gtrsim$400 km s^{-1}) are seen at the nucleus, and along the east-west direction. Regions to the north and south of the nucleus present low $W_{80\,H_2}$ values ($\lesssim$200 km s^{-1}).

4. DISCUSSION

In this work, we investigate the origin of the excess H_2 emission in three galaxies: 3C 293, which hosts a radio-loud AGN, and NGC 3884 and CGCG 012-070, both hosting radio-quiet AGNs (Becker et al. 1995; Liu & Zhang 2002; Lofthouse et al. 2018; Lin et al. 2018; Kukreti et al. 2022).

Strong mid-IR H_2 emission has been previously reported in radio-loud AGN hosts. For instance, Spitzer observations of the FR II radio galaxy 3C 326 reveal exceptionally strong H_2 shock-heated emission from its northern component, with the total integrated luminosity of the H_2 pure rotational transitions corresponding to 17 % of the galaxy's 8-70 μm luminosity (Ogle et al. 2007). The importance of the radio jet in powering the outflow in 3C 326N and line emission through interactions between different phases of the ISM gas is reinforced by Nesvadba et al. (2010), using CO (1-0) interferometric and Spitzer observations. They conclude that AGN feedback potentially lowers the star formation efficiency in a way that is consistent with observations of other H_2-luminous radio galaxies, with small ratios of CO and PAH surface brightness. Ogle et al. (2010), using a sample of 55 radio galaxies at redshift $z < 0.22$ (including 3C 293) observed with the Spitzer satellite, found that 31 % of them exhibit pure-rotational H_2 emission lines, with molecular masses reaching up to 2×10^{10} M$_\odot$ and $L_{H_2}/L_{PAH\,7.7\,\mu m}$ ratios approximately 300 times higher than those in normal star-forming galaxies. The authors suggest that the H_2 emission in these radio-selected molecular hydrogen emission galaxies (MOHEGs) is caused by heating from radio jets. This conclusion is reinforced by deep Spitzer observations of radio galaxies with neutral and ionized gas outflows (including 3C 293) show that the radio jet, which drives the outflow, is also responsible for the shock excitation of the warm H_2 gas (Guillard et al. 2012). Modeling the spectral energy distributions from ultraviolet to far-infrared of radio galaxies (including 3C 293) – selected for the presence of shocked, warm molecular hydrogen emission – indicates that star formation is suppressed due to shocks driven by the radio jets, which also powers the luminous warm H_2 line emission (Lanz et al. 2016). Chandra observations of 3C 293 reveal X-ray emission from the jets both within the host galaxy and along the 100 kpc radio jets. The thermal X-ray and warm H_2 luminosities are comparable, indicating similar masses of X-ray hot gas and warm molecular gas. This suggests that both components originate from a multiphase, shocked ISM (Lanz et al. 2015). Multiwavelength imaging and spectroscopy of M 58 indicate that much of the molecular gas is shocked in situ within the radio jet cocoon, supporting a scenario where jet-driven shocks significantly reduce star formation in the central region of galaxies (Ogle et al. 2024).

The studies above reinforce the importance of shocks driven by radio jets in the production of extremely strong H_2 rotational lines in radio galaxies, which can now be studied in more details with JWST. MIRI MRS observations of IC 5063, a galaxy where the radio jet intercepts the gaseous disk, reveal that the warm H_2 is most excited in regions that are co-spatial with the radio structures (Dasyra et al. 2024). MIRI MRS observations also revealed jet-driven outflows in warm molecular gas in the inner central regions of 3C 326 N (Leftley et al. 2024) and 3C 293 (Costa-Souza et al. 2024), with evidence of shock-heated H_2 gas, associated to radio emission.

Shocks also appear to play a significant role in the production of H_2 emission in nearby Seyfert and LINER host galaxies. For instance, Ogle et al. (2014) found that the rotational H_2 emission from the Seyfert host NGC 4258 originates from its inner anomalous arms, which is

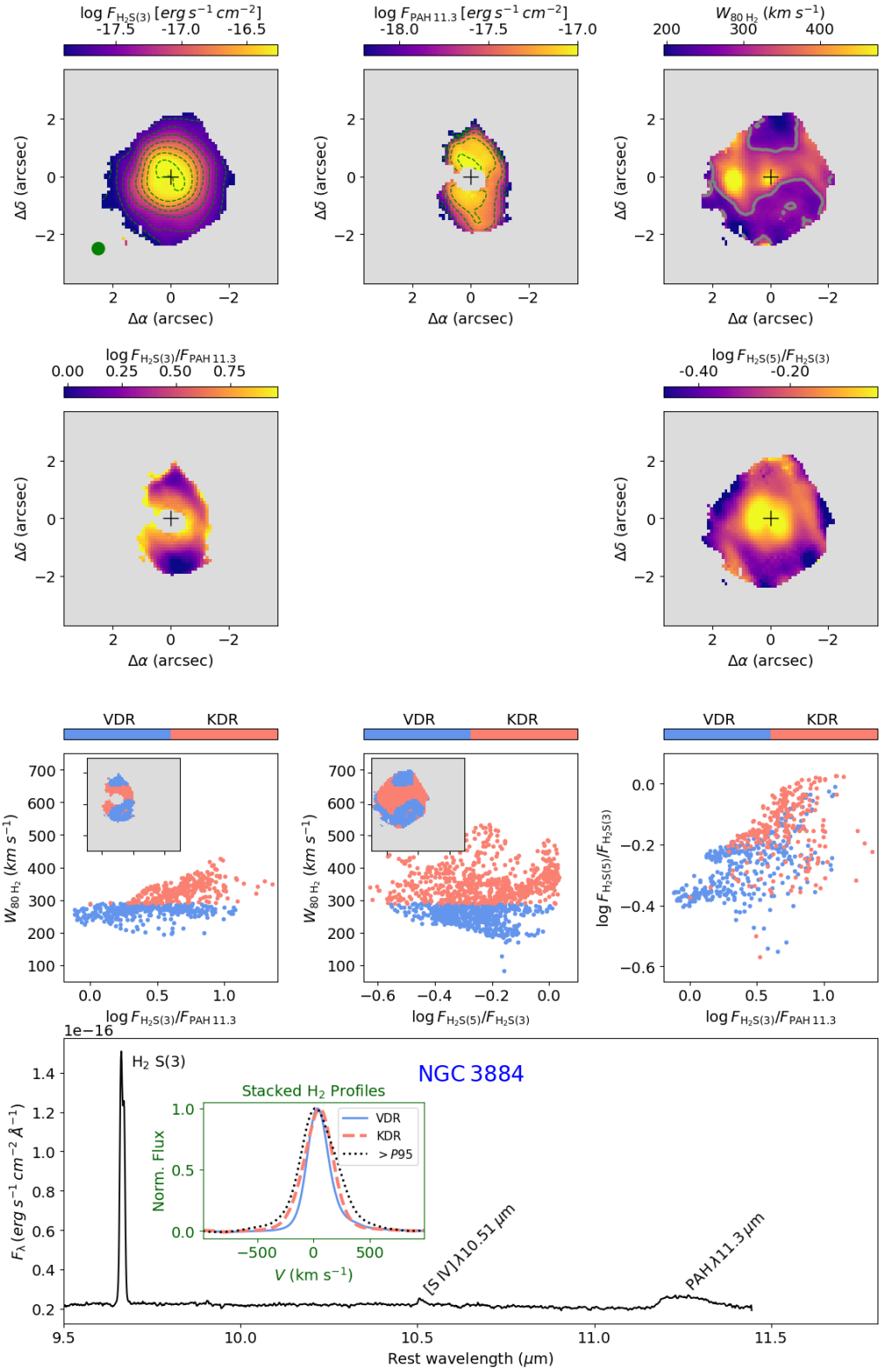

Figure 4. Same as Fig. 2, but for NGC 3884. The $[\mathrm{Fe\,II}]_{5.34\,\mu m}/\mathrm{PAH}_{11.3\mu m}$ line ratio map is not shown for this galaxy, because the observed spectral range does not include the $[\mathrm{Fe\,II}]_{5.34\,\mu m}$ emission line. Radio contours are not shown as there are no high resolution radio data available for this object.

a signature of jet interaction with the galaxy disk. Additionally, they report a large $L_{H_2}/L_{PAH\,7.7\,\mu m}$ of 0.37, typical of MOHEGs, indicating shocked molecular gas emission. García-Bernete et al. (2024) use MIRI/MRS observations of the inner ∼kpc of three nearby AGN hosts from the Galactic Activity, Torus, and Outflow Survey (GATOS) map the PAH and H_2 MIR flux distributions. They find spatially resolved differences of the H_2/PAH ratio for AGN and star-forming dominated regions, with the highest values observed in AGN dominated regions and the lowest ones in the SF dominated regions. Additionally, the AGN radiation and outflows may influence the PAH population at nuclear and kpc scales, particularly regarding the ionization state of the PAH grains, although their molecular sizes remain relatively similar (García-Bernete et al. 2024).

The importance of shocks in driving H_2 MIR emission in nearby galaxies is further supported by studies of gas kinematics through optical spectroscopy and radio observations. In addition to exhibiting higher H_2/PAH ratios, AGN host galaxies also show elevated H_2 excitation temperatures compared to normal galaxies (e.g. Petric et al. 2018; Lambrides et al. 2019). Riffel et al. (2020b) investigated the optical properties of a sample composed of 309 nearby galaxies from a parent sample of 2015 objects observed with the Spitzer Telescope, from Lambrides et al. (2019). These authors found that the kinematics of [O I]λ6300 emission in AGN hosts cannot be explained solely by gas motions resulting from the gravitational potential of their host galaxies, requiring an outflow component. They also observed a correlation between the H_2 S(3)/PAH 11.3 μm ratio and the [O I] line width, as well as with the [O I]/Hα ratio, a well-known tracer of shocks in neutral gas. This provides an indirect evidence that the H_2 emission excess, observed in AGN hosts, is associated to shocks in the same clouds that produce the [O I] emission (Riffel et al. 2020b). Spatially resolved ALMA observations of cold molecular gas in individual sources reveal that highly disturbed cold gas is closely associated with strong H_2 emission and is co-spatial with radio jets (Nesvadba et al. 2021; Ogle et al. 2024). This indicates that the H_2 emission is generated by shocks resulting from the energy injected into the ISM by radio jets and outflows. Evidence of shock-heated gas emission in galaxies with H_2 emission excess is also observed in hot molecular, neutral and ionized gas through optical and near-infrared integral field spectroscopy (e.g. Colina et al. 2015; Riffel et al. 2020a, 2023a, 2024)

Except for the results obtained with JWST, most of the findings discussed above are based on integrated observations or imaging of H_2 transitions, with limited kinematic information, or rely on indirect tracers such as cold molecular gas observed in the radio or neutral and ionized gas in the optical. Our results allow for a detailed discussion of the origin of H_2 emission in the three observed galaxies, mapping both the flux distribution and kinematics in a spatially resolved manner. For the three galaxies studied here, the maps of the H_2 S(3)/PAH$_{11.3\mu m}$ and [Fe II]$_{5.34\,\mu m}$/PAH$_{11.3\mu m}$ line ratios exhibit similar patterns among them, for each object. The [Fe II] emission is a well-known indicator of shocks. Shocks destroy dust grains, releasing iron (Fe) and increasing its abundance, thereby enhancing its emission (e.g. Oliva et al. 2001; Storchi-Bergmann et al. 2009; Riffel et al. 2013, 2010; Hill & Zakamska 2014; Colina et al. 2015; Riffel et al. 2021a). In addition, these galaxies were selected as having high values of [O I]λ6300/Hα ratios, with $\log$ [O I]λ6300/H$\alpha \approx -0.69$ for 3C 293, $\log$ [O I]λ6300/H$\alpha \approx -0.51$ for CGCG 012-070, and $\log$ [O I]λ6300/H$\alpha \approx -0.38$ for NGC 3884 (Riffel et al. 2020b). The [O I]λ6300 is also a well-known shock tracer in neutral gas (Monreal-Ibero et al. 2006, 2010; Rich et al. 2011, 2015), with shocks being the dominant excitation mechanism for galaxies with $\log$ [O I]λ6300/H$\alpha \gtrsim -1.5$ and [O I]λ6300 velocity dispersion (σ_{OI}) of at least 150 km s^{-1} (e.g. Allen et al. 2008; Ho et al. 2014). The three galaxies have $\sigma_{OI} > 220$ km s^{-1}, as measured from their SDSS spectra (Riffel et al. 2020b). Therefore, these results indicate that, at least partially, the observed H_2 line emission in these galaxies is likely due to H_2 molecule excitation by shocks.

The plots of W_{80H_2} vs. $\log$ H_2 S(3)/PAH$_{11.3\mu m}$ shown in Figs. 2, 3 and 4 clearly present two trends for all galaxies: (i) one group of points where the H_2 S(3)/PAH$_{11.3\mu m}$ ratio increases with W_{80H_2}, and (ii) another group of points where the ratio remains practically constant. A correlation between the W_{80H_2} with H_2 S(3)/PAH$_{11.3\mu m}$ may indicate a kinematic evidence that shocks are producing the H_2 emission excess observed in these galaxies. To roughly distinguish between the two groups of points and spatially locate them within the galaxies, we follow Riffel et al. (2023b) and identify the kinematically disturbed regions (KDRs) and the virially dominated region (VDRs), using the W_{80} measurements. When gas motion is primarily driven by the gravitational potential, the velocity dispersion is expected to decline with increasing distance from the nucleus. Consequently, the velocity dispersion observed at the nucleus can be interpreted as the upper limit of what is attributable to the gravitational potential. We establish a threshold to define the KDR, based on the fitting of the H_2 S(3) emission-line nuclear profile. For each

galaxy, we model the H_2 S(3) emission line in the nuclear spaxel using two Gaussian components: a narrow component attributed to gas in the plane of the disc, and a broad component associated with outflows. The KDR correspond to locations with W_{80} values larger than that of the nuclear narrow component, while other locations corresponds to the VDR, defined by spaxels with W_{80} values smaller than the nuclear one. The W_{80} limits are 370 km s^{-1} for 3C 293, 290 km s^{-1} for NGC 3884 and 385 km s^{-1} for CGCG 012-070. The uncertainties in the values of the nuclear narrow component W_{80} are less than 20 km s^{-1} for all three galaxies, resulting in an effect of less than ∼5 % on the fraction of spaxels that define the KDR in all objects. As discussed in Riffel et al. (2023b), for nearby AGN hosts, the different assumptions used to select spaxels and calculate the mass of the outflow gas lead to discrepancies of up to 1 dex in the ionized gas outflow rates between different methods, with approximately 0.3 dex of this discrepancy due to the limits W_{80} used to define the spaxels dominated by outflows.

The W_{80} cuts are below the escape velocity for all three galaxies. Using SDSS-based stellar masses (Maraston et al. 2009) and isophotal radii (Adelman-McCarthy et al. 2008), and assuming that the stellar mass corresponds to 15% of the total mass of the galaxies, we obtain rough escape velocities of 460 km s^{-1} for 3C 293, 540 km s^{-1} for NGC 3884, and 445 km s^{-1} for CGCG 012-070, estimated using a simple Keplerian approximation. For all three galaxies, the W_{80} limits used to separate the KDR from the VDR are lower than the escape velocities. In 3C 293, 26% of the KDR spaxels have velocities above the escape velocity, which accounts for ∼51% of the H_2 S(3) emission line flux in the KDR. None of the spaxels in NGC 3884 exceed the escape velocity, while 62% of the KDR spaxels in CGCG 012-070 have velocities above the escape velocity, accounting for 33% of the H_2 S(3) KDR emission.

For 3C 293, there is a clear trend of W_{80H_2} increasing with log H2 S(3)/PAH11.3μm in the KDR (Fig. 2). A similar behavior is observed in the other two galaxies, although it is less pronounced (Figs. 3 and 4). The increase in the H_2/PAH ratio with the H_2 line width may indicate that shocks play a significant role in the excitation of the H_2 molecule, as larger line widths trace more turbulent gas. This is consistent with results obtained for AGN hosts using Spitzer observations and indirect indicators of gas turbulence derived from optical and radio emission lines, commonly attributed to shocks associated with radio jets (e.g. Nesvadba et al. 2010, 2021; Ogle et al. 2010, 2024; Riffel et al. 2020b) and by recent MIRI MRS observations of nearby AGN hosts (Leftley et al. 2024; García-Bernete et al. 2024; Dasyra et al. 2024).

The H_2 S(5)/H_2 S(3) emission line ratio is a tracer of the gas temperature, representing a fraction of hotter-to-colder molecular gas. In all galaxies, the highest values of this ratio is observed is seen co-spatial with the highest H2 S(3)/PAH11.3μm regions. For 3C 293 there is a clear correlation between the H_2 S(5)/H_2 S(3) and H_2 S(3) line width and the log H2 S(5)/H2 S(5) vs. log H2 S(3)/PAH11.3μm plot shows a similar bimodal behaviour as seen in W_{80H_2} vs. log H_2 S(3)/PAH$_{11.3\mu m}$ plot roughly separating the VDR and KDR. In addition, the highest values of all line ratios and W_{80H_2} are co-spatial with the radio core (Kukreti et al. 2022). This indicates that the outflows in 3C 293 are driven by the radio jet – as previously reported (Mahony et al. 2016; Riffel et al. 2023a; Costa-Souza et al. 2024) and the H_2 emission from the KDR is produced by shock excitation. CGCG 012-070 and NGC 3884 also show the highest H_2 S(5)/H_2 and H_2 S(3)/PAH11.3μm line ratios in co-spatial regions, with a trend suggesting that the increases in both ratios are closely linked. These two galaxies do not show a clear trend of higher H_2 S(5)/H_2 S(3) ratios (indicating hotter gas) being associated with line widths (more turbulent gas), and they also do not have radio images with similar resolution to our data, despite being detected by the VLA FIRST survey (Becker et al. 1995; Lofthouse et al. 2018; Lin et al. 2018). This suggests that the contribution of shocks to the excitation of H_2 mid-infrared lines is less significant compared to 3C 293, but still not negligible for the two galaxies, in particular for the KDR.

The insets in the bottom panels of Figs 2, 3 and 4 show stacked H_2 S(3) emission line profiles for the KDR (in salmon) and in the VDR (blue) for the three galaxies. These profiles were created by summing all spaxels in each region, using the centroid velocity of the line as the reference, and then normalizing them by the peak of the profile. The line profiles in the KDRs are more asymmetric than those in the VDRs. In the case of CGCG 012-070, the line profiles from both regions show similar widths and exhibit a blueshifted asymmetric wing. Although the distribution in the W_{80H_2} versus H2 S(3)/PAH11.3μm plot is bimodal for this galaxy (Fig. 3), correlations between these parameters are observed in both groups of points. This suggests that shocks contribute additionally in the VDR of CGCG 012-070.

We can further investigate the role of shocks in the excitation of the H_2 gas, using the observed luminosities of the H_2 emission lines and adopting a power-law temperature distribution (Zakamska 2010; Pereira-Santaella

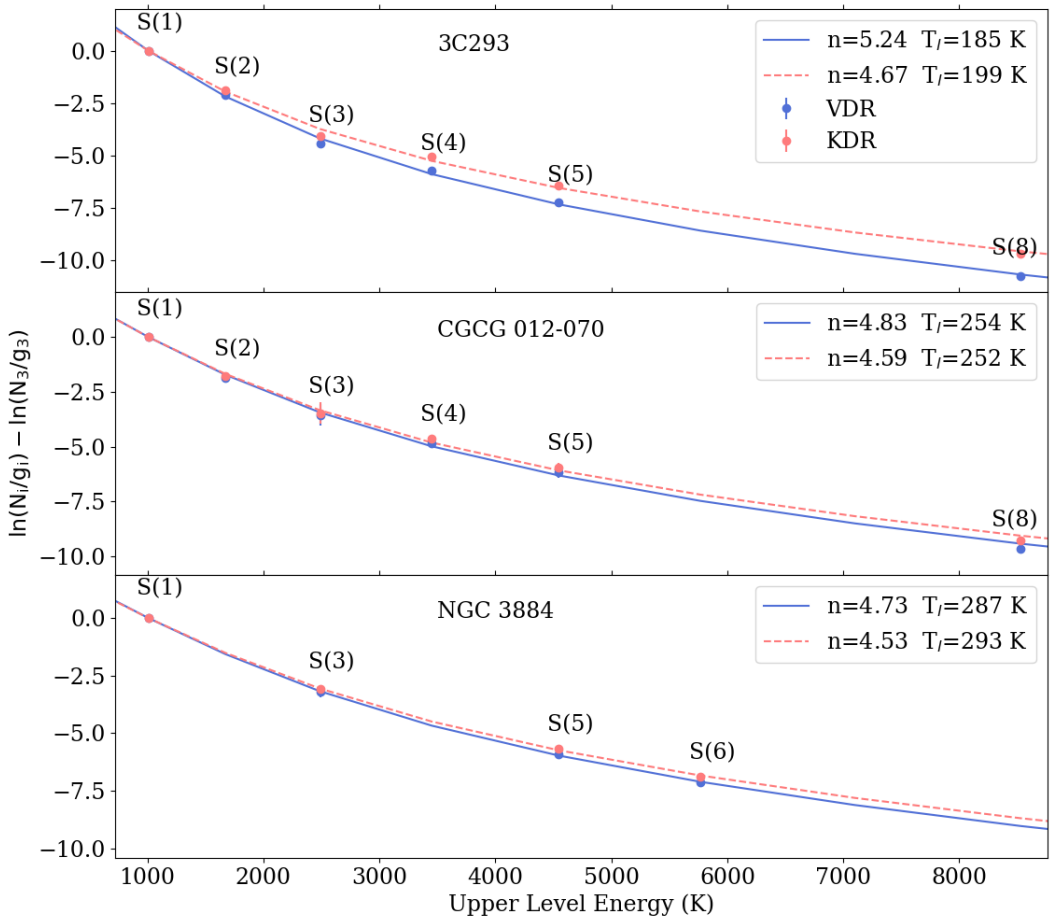

Figure 5. Excitation diagrams for the VDR and KDR in 3C 293 (top), CGCG 012-070 (middle) and NGC 3884 (bottom). The points are obtained from the integrated H_2 fluxes, while the lines correspond to the best-fitted power-law temperature model.

et al. 2014; Togi & Smith 2016). We follow the procedure described in Costa-Souza et al. (2024), evaluating the column density of the J state (N_J) by

$$N_J = \int_{T_u}^{T_l} f(T) m T^{-n} dT, \quad (1)$$

where m is a normalization constant $f(T)$ is the Boltzmann factor, T_u and T_l are the upper and lower temperature limits and n is the power-law index. Figure 5 shows the excitation for the three galaxies in our sample, using all the observed H_2 transitions detected in their spectra. The plots display on the y-axis the population number of the i state divided by the state degeneracy and normalized by the $i = 3$ state, while the x-axis represents the upper level energy. We compute the integrated fluxes for each H_2 emission line for the KDR and VDR, considering spaxels where all emission lines are detected. We corrected the observed fluxes for extinction using the G23 extinction law (Gordon et al. 2023, 2021, 2009; Gordon 2024; Decleir et al. 2022; Fitzpatrick et al. 2019) and mean visual extinctions (A_V) of 2.6, 1.4, and 0.8 mag, estimated from the Balmer decrement using Hα and Hβ flux measurements from Thomas et al. (2013) for 3C 293, CGCG 012-070, and NGC 3884, respectively. The best fit models are shown as salmon and blue lines for the KDR and VDR, respectively. To obtain the best model, we kept $T_u = 5000$ K fixed (Yuan & Neufeld 2011) and varied the other two parameters, T_l and n. The best-fit parameters are shown in the top-right corner of the plots, for each galaxy.

If molecular gas is heated by shocks, a flat power-law index is expected, resulting in higher temperatures that favor a larger fraction of gas being in hotter phases compared to gas in photodissociation regions (Togi & Smith 2016). For instance, Togi & Smith (2016) reported power-law index values in the range 3.79–6.39, and a mean value of $\langle n \rangle = 4.84 \pm 0.61$, for a sample of 43 galaxies from the Spitzer Infrared Nearby Galaxies Survey (SINGS, Kennicutt et al. 2003), which include LINERs, Seyferts, Dwarfs, and Star-forming galaxies. Considering only the Star-formation dominated galaxies (18) in their sample, the mean value is $\langle n \rangle = 5.16 \pm 0.36$, while

considering only AGN (Seyferts and LINERs) hosts (20) the mean index is $\langle n \rangle = 4.46 \pm 0.44$. Appleton et al. (2017) present a two-dimensional map of the power-law index for the Stephan's Quintet, based on Spitzer images. They found values in the range ∼4.2–5.0, with the lowest values observed in shock dominated regions. The same range of n values is reported by Appleton et al. (2023) using JWST MIRI observations. ULIRGs typically exhibit power-law index values within the range 2.5–5.0, with lower values associated to shock dominated regions (e.g. Zakamska 2010). As shown in Figure 5, the KDR in the three galaxies exhibits lower n values compared to the VDR, with the largest difference seen for 3C 293. This confirms that shocks play a major role in the observed emission from the kinematically disturbed region.

We can speculate on the origin of the shocks. The three galaxies studied here include different representatives of AGNs regarding the radio emission and optical classification. NGC 3884 hosts a type 1 LINER, CGCG 012-070 hosts a Sy 2 nucleus, and 3C 293 hosts a LINER (Véron-Cetty & Véron 2006). 3C 293 is a radio loud source, whereas NGC 3884 and CGCG 012-070 are radio quiet, but presenting faint radio emission (Liu & Zhang 2002; Becker et al. 1995; Lofthouse et al. 2018; Lin et al. 2018). In addition these galaxies present outflows in ionized gas, which seem to be mechanically driven by the interaction of the radio jet with the ambient gas in the 3C 293 and likely radiatively driven in the other two, as they show only faint radio emission (Riffel et al. 2023a, 2024). The shock-dominated regions are seen mostly in the central region for all galaxies. In addition, the shock-dominated region in 3C 293 is seen co-spatial with the radio core, indicating that the origin of the shocks is the interaction of the radio jet with the ambient gas, in agreement with previous results using Spitzer observations and indirect tracers of the warm H_2 emission (Ogle et al. 2010; Guillard et al. 2012; Lanz et al. 2015). The jet-cloud interaction is also responsible for driving the warm molecular and ionized gas outflows in this object (Mahony et al. 2016; Riffel et al. 2023a; Costa-Souza et al. 2024). Since NGC 3884 and CGCG 012-070 exhibit only weak radio emission, the origin of the shocks in these galaxies is likely due to radiatively driven outflows. However, because of the lack of high-sensitivity radio observations for these galaxies, low-power jets cannot be ruled out as the potential source of their shock-heated H_2 emission. Indeed, interactions between low-power radio jets and the interstellar medium are the source of the outflows observed in ionized gas in nearby AGN hosts (Nandi et al. 2023; Girdhar et al. 2024). This interpretation aligns with predictions from simulations indicating that molecules can form within outflows, with their emission attributed to shock heating (Richings & Faucher-Giguère 2018a,b).

5. CONCLUSIONS

We used JWST MIRI MRS observations of the inner ∼2 kpc of the nearby AGN hosts 3C 293, CGCG 012-070 and NGC 3884 to investigate the origin of the H_2 emission excess observed in these galaxies. Our main conclusions are:

- The median values of $\log \mathrm{H_2\ S(3)/PAH_{11.3\mu m}}$ observed for 3C 293, CGCG 012-070, and NGC 3884 are 0.15, 0.35, and 3.32, respectively. These values significantly exceed those measured for non-active galaxies using Spitzer data, which have a median value of $\log \mathrm{H_2\ S(3)/PAH_{11.3\mu m}} = -1.74$, as well as the median values for AGN hosts, which are typically around $\log \mathrm{H_2\ S(3)/PAH_{11.3\mu m}} = -1.26$. This places these galaxies among the most extreme cases of H_2 emission excess.

- Plots of $W_{80\mathrm{H_2}}$ vs. $\log \mathrm{H_2\ S(3)/PAH_{11.3\mu m}}$ clearly exhibit two trends in all galaxies: (i) one cluster of points where the H_2 S(3)/PAH$_{11.3\mu m}$ ratio and $W_{80\mathrm{H_2}}$ present a strong correlation, and (ii) another cluster with the ratio remaining nearly constant.

- Using the $W_{80\mathrm{H_2}}$ values, we define the kinematically disturbed region (KDR) and the virially dominated region (VDR), and find that shock heating of the gas is the primary excitation mechanism for H_2 emission in the KDR. This is supported by larger fractions of hotter-to-colder molecular gas (traced by the H_2 S(5)/H_2 S(3) ratio), a correlation between the H_2 and [Fe II] and flatter power-law temperature distributions in the KDR, as compared to the VDR.

- The origin of the shocks in 3C 293 is the interaction between the radio jet and the interstellar medium, as indicated by the spatial correlation between the radio emission and the highest line ratio values and warm molecular jet-driven outflows. The other two galaxies exhibit modest radio emission; however, the interaction of low-power jets with the interstellar medium cannot be ruled out as a potential source of the shocks. Higher sensitivity radio observations are necessary to further investigate the role of the radio jet in the origin of the excess H_2 emission in these galaxies.

Our work demonstrates the capability of the JWST MIRI MRS in investigating the origin of H_2 emission

excess in nearby AGN hosts, as revealed by Spitzer observations. While Spitzer's limited spatial and spectral resolutions constrained our ability to disentangle shock and AGN heating processes, JWST now provides the detailed spatial and spectral information necessary to understand the formation and origins of molecular emission, as well as its relationship with outflows.

ACKNOWLEDGMENTS

We would like to thank an anonymous referee for their contributions, which greatly improved the presentation of this manuscript. RAR acknowledges the support from Conselho Nacional de Desenvolvimento Científico e Tecnológico (CNPq; Proj. 303450/2022-3, 403398/2023-1, & 441722/2023-7), Fundação de Amparo à pesquisa do Estado do Rio Grande do Sul (FAPERGS; Proj. 21/2551-0002018-0), and Coordenação de Aperfeiçoamento de Pessoal de Nível Superior (CAPES; Proj. 88887.894973/2023-00). HCPS and GLSO thank the financial support from CAPES (Finance Code 001) and CNPq. N.L.Z. is supported in part by NASA through STScI grant JWST-ERS-01928. RR acknowledges support from CNPq (Proj. 311223/2020-6, 304927/2017-1, 400352/2016-8, and 404238/2021-1), FAPERGS (Proj. 19/1750-2 and 24/2551-0001282-6) and (CAPES, Proj. Proj. 88887.894973/2023-00). MB thanks the financial support from the IAU-Gruber foundation fellowship.

DATA AVAILABILITY

The data used in this work are part of the JWST cycle 1 project (ID 1928). The complete dataset can be accessed at the Mikulski Archive for Space Telescopes (MAST) platform at the Space Telescope Science Institute, through 10.17909/tazj-hp44.

Facilities: JWST (MIRI MRS), MAST, NED.

REFERENCES

Adelman-McCarthy, J. K., Agüeros, M. A., Allam, S. S., et al. 2008, ApJS, 175, 297, doi: 10.1086/524984

Allen, M. G., Groves, B. A., Dopita, M. A., Sutherland, R. S., & Kewley, L. J. 2008, ApJS, 178, 20, doi: 10.1086/589652

Alonso-Herrero, A., García-Burillo, S., Pereira-Santaella, M., et al. 2019, A&A, 628, A65, doi: 10.1051/0004-6361/201935431

Appleton, P. N., Guillard, P., Togi, A., et al. 2017, ApJ, 836, 76, doi: 10.3847/1538-4357/836/1/76

Appleton, P. N., Guillard, P., Emonts, B., et al. 2023, ApJ, 951, 104, doi: 10.3847/1538-4357/accc2a

Argyriou, I., Glasse, A., Law, D. R., et al. 2023a, A&A, 675, A111, doi: 10.1051/0004-6361/202346489

—. 2023b, A&A, 675, A111, doi: 10.1051/0004-6361/202346489

Becker, R. H., White, R. L., & Helfand, D. J. 1995, ApJ, 450, 559, doi: 10.1086/176166

Bushouse, H., Eisenhamer, J., Dencheva, N., et al. 2024, JWST Calibration Pipeline, 1.14.0, Zenodo, doi: 10.5281/zenodo.10870758

Cazzoli, S., Márquez, I., Masegosa, J., et al. 2018, MNRAS, 480, 1106, doi: 10.1093/mnras/sty1811

Colina, L., Piqueras López, J., Arribas, S., et al. 2015, A&A, 578, A48, doi: 10.1051/0004-6361/201425567

Costa-Souza, J. H., Riffel, R. A., Souza-Oliveira, G. L., et al. 2024, ApJ, 974, 127, doi: 10.3847/1538-4357/ad702a

Dasyra, K. M., Paraschos, G. F., Combes, F., et al. 2024, arXiv e-prints, arXiv:2406.03218, doi: 10.48550/arXiv.2406.03218

Davies, R., Shimizu, T., Pereira-Santaella, M., et al. 2024, arXiv e-prints, arXiv:2406.17072, doi: 10.48550/arXiv.2406.17072

de Vaucouleurs, G., de Vaucouleurs, A., Corwin, Herold G., J., et al. 1991, Third Reference Catalogue of Bright Galaxies

Decleir, M., Gordon, K. D., Andrews, J. E., et al. 2022, ApJ, 930, 15, doi: 10.3847/1538-4357/ac5dbe

Dors, O. L., Contini, M., Riffel, R. A., et al. 2021, MNRAS, 501, 1370, doi: 10.1093/mnras/staa3707

Ebneter, K., & Balick, B. 1985, AJ, 90, 183, doi: 10.1086/113724

Eisenstein, D. J., Weinberg, D. H., Agol, E., et al. 2011, AJ, 142, 72, doi: 10.1088/0004-6256/142/3/72

Emonts, B. H. C., Morganti, R., Tadhunter, C. N., et al. 2005, MNRAS, 362, 931, doi: 10.1111/j.1365-2966.2005.09354.x

Fanaroff, B. L., & Riley, J. M. 1974, MNRAS, 167, 31P, doi: 10.1093/mnras/167.1.31P

Fitzpatrick, E. L., Massa, D., Gordon, K. D., Bohlin, R., & Clayton, G. C. 2019, ApJ, 886, 108, doi: 10.3847/1538-4357/ab4c3a

García-Bernete, I., Rigopoulou, D., Donnan, F. R., et al. 2024, A&A, 691, A162, doi: 10.1051/0004-6361/202450086

Girdhar, A., Harrison, C. M., Mainieri, V., et al. 2024, MNRAS, 527, 9322, doi: 10.1093/mnras/stad3453

Gordon, K. 2024, The Journal of Open Source Software, 9, 7023, doi: 10.21105/joss.07023

Gordon, K. D., Cartledge, S., & Clayton, G. C. 2009, ApJ, 705, 1320, doi: 10.1088/0004-637X/705/2/1320

Gordon, K. D., Clayton, G. C., Decleir, M., et al. 2023, ApJ, 950, 86, doi: 10.3847/1538-4357/accb59

Gordon, K. D., Misselt, K. A., Bouwman, J., et al. 2021, ApJ, 916, 33, doi: 10.3847/1538-4357/ac00b7

Guillard, P., Ogle, P. M., Emonts, B. H. C., et al. 2012, ApJ, 747, 95, doi: 10.1088/0004-637X/747/2/95

Gunn, J. E., Siegmund, W. A., Mannery, E. J., et al. 2006, AJ, 131, 2332, doi: 10.1086/500975

Hermosa Muñoz, L., Márquez, I., Cazzoli, S., Masegosa, J., & Agís-González, B. 2022, A&A, 660, A133, doi: 10.1051/0004-6361/202142629

Hernandez, S., Jones, L., Smith, L. J., et al. 2023, ApJ, 948, 124, doi: 10.3847/1538-4357/acc837

Hill, M. J., & Zakamska, N. L. 2014, MNRAS, 439, 2701, doi: 10.1093/mnras/stu123

Ho, I. T., Kewley, L. J., Dopita, M. A., et al. 2014, MNRAS, 444, 3894, doi: 10.1093/mnras/stu1653

Kautsch, S. J., Grebel, E. K., Barazza, F. D., & Gallagher, J. S., I. 2006, A&A, 445, 765, doi: 10.1051/0004-6361:20053981

Kennicutt, Robert C., J., Armus, L., Bendo, G., et al. 2003, PASP, 115, 928, doi: 10.1086/376941

Kukreti, P., Morganti, R., Shimwell, T. W., et al. 2022, A&A, 658, A6, doi: 10.1051/0004-6361/202140814

Labiano, A., García-Burillo, S., Combes, F., et al. 2014, A&A, 564, A128, doi: 10.1051/0004-6361/201323123

Labiano, A., Argyriou, I., Álvarez-Márquez, J., et al. 2021, A&A, 656, A57, doi: 10.1051/0004-6361/202140614

Lambrides, E. L., Petric, A. O., Tchernyshyov, K., Zakamska, N. L., & Watts, D. J. 2019, MNRAS, 487, 1823, doi: 10.1093/mnras/stz1316

Lanz, L., Ogle, P. M., Alatalo, K., & Appleton, P. N. 2016, ApJ, 826, 29, doi: 10.3847/0004-637X/826/1/29

Lanz, L., Ogle, P. M., Evans, D., et al. 2015, ApJ, 801, 17, doi: 10.1088/0004-637X/801/1/17

Leftley, J. H., Nesvadba, N. P. H., Bicknell, G. V., et al. 2024, A&A, 689, A314, doi: 10.1051/0004-6361/202449848

Lin, Y.-T., Huang, H.-J., & Chen, Y.-C. 2018, AJ, 155, 188, doi: 10.3847/1538-3881/aab5b4

Liu, F. K., & Zhang, Y. H. 2002, A&A, 381, 757, doi: 10.1051/0004-6361:20011572

Lofthouse, E. K., Kaviraj, S., Smith, D. J. B., & Hardcastle, M. J. 2018, MNRAS, 479, 807, doi: 10.1093/mnras/sty1375

Machalski, J., Jamrozy, M., Stawarz, Ł., & Weżgowiec, M. 2016, A&A, 595, A46, doi: 10.1051/0004-6361/201629249

Mahony, E. K., Oonk, J. B. R., Morganti, R., et al. 2016, MNRAS, 455, 2453, doi: 10.1093/mnras/stv2456

Maraston, C., Strömbäck, G., Thomas, D., Wake, D. A., & Nichol, R. C. 2009, MNRAS, 394, L107, doi: 10.1111/j.1745-3933.2009.00621.x

Martel, A. R., Baum, S. A., Sparks, W. B., et al. 1999, ApJS, 122, 81, doi: 10.1086/313205

Monreal-Ibero, A., Arribas, S., & Colina, L. 2006, ApJ, 637, 138, doi: 10.1086/498257

Monreal-Ibero, A., Arribas, S., Colina, L., et al. 2010, A&A, 517, A28, doi: 10.1051/0004-6361/200913239

Morganti, R., Oosterloo, T. A., Emonts, B. H. C., van der Hulst, J. M., & Tadhunter, C. N. 2003, ApJL, 593, L69, doi: 10.1086/378219

Nair, P. B., & Abraham, R. G. 2010, ApJS, 186, 427, doi: 10.1088/0067-0049/186/2/427

Nandi, P., Stalin, C. S., Saikia, D. J., et al. 2023, ApJ, 959, 116, doi: 10.3847/1538-4357/ad0c57

Nesvadba, N. P. H., Boulanger, F., Salomé, P., et al. 2010, A&A, 521, A65, doi: 10.1051/0004-6361/200913333

Nesvadba, N. P. H., Wagner, A. Y., Mukherjee, D., et al. 2021, A&A, 654, A8, doi: 10.1051/0004-6361/202140544

Ogle, P., Antonucci, R., Appleton, P. N., & Whysong, D. 2007, ApJ, 668, 699, doi: 10.1086/521334

Ogle, P., Boulanger, F., Guillard, P., et al. 2010, ApJ, 724, 1193, doi: 10.1088/0004-637X/724/2/1193

Ogle, P. M., Lanz, L., & Appleton, P. N. 2014, ApJL, 788, L33, doi: 10.1088/2041-8205/788/2/L33

Ogle, P. M., López, I. E., Reynaldi, V., et al. 2024, ApJ, 962, 196, doi: 10.3847/1538-4357/ad1242

Ogle, P. M., Sebastian, B., Aravindan, A., et al. 2025, arXiv e-prints, arXiv:2502.06603, doi: 10.48550/arXiv.2502.06603

Oliva, E., Marconi, A., Maiolino, R., et al. 2001, A&A, 369, L5, doi: 10.1051/0004-6361:20010214

Omont, A. 2007, Reports on Progress in Physics, 70, 1099, doi: 10.1088/0034-4885/70/7/R03

Pereira-Santaella, M., Spinoglio, L., van der Werf, P. P., & Piqueras López, J. 2014, A&A, 566, A49, doi: 10.1051/0004-6361/201423430

Pereira-Santaella, M., Álvarez-Márquez, J., García-Bernete, I., et al. 2022, A&A, 665, L11, doi: 10.1051/0004-6361/202244725

Petric, A. O., Armus, L., Flagey, N., et al. 2018, AJ, 156, 295, doi: 10.3847/1538-3881/aaca35

Rich, J. A., Kewley, L. J., & Dopita, M. A. 2011, ApJ, 734, 87, doi: 10.1088/0004-637X/734/2/87

—. 2015, ApJS, 221, 28, doi: 10.1088/0067-0049/221/2/28

Richings, A. J., & Faucher-Giguère, C.-A. 2018a, MNRAS, 474, 3673, doi: 10.1093/mnras/stx3014

—. 2018b, MNRAS, 478, 3100, doi: 10.1093/mnras/sty1285

Riffel, R., Rodríguez-Ardila, A., Aleman, I., et al. 2013, MNRAS, 430, 2002, doi: 10.1093/mnras/stt026

Riffel, R. A., Bianchin, M., Riffel, R., et al. 2021a, MNRAS, 503, 5161, doi: 10.1093/mnras/stab788

Riffel, R. A., Riffel, R., Bianchin, M., et al. 2023a, MNRAS, 521, 3260, doi: 10.1093/mnras/stad776

Riffel, R. A., Riffel, R., Storchi-Bergmann, T., et al. 2024, MNRAS, 528, 1476, doi: 10.1093/mnras/stae055

Riffel, R. A., Storchi-Bergmann, T., & Nagar, N. M. 2010, MNRAS, 404, 166, doi: 10.1111/j.1365-2966.2010.16308.x

Riffel, R. A., Storchi-Bergmann, T., Zakamska, N. L., & Riffel, R. 2020a, MNRAS, 496, 4857, doi: 10.1093/mnras/staa1922

Riffel, R. A., Vale, T. B., Storchi-Bergmann, T., & McGregor, P. J. 2014, MNRAS, 442, 656, doi: 10.1093/mnras/stu843

Riffel, R. A., Zakamska, N. L., & Riffel, R. 2020b, MNRAS, 491, 1518, doi: 10.1093/mnras/stz3137

Riffel, R. A., Storchi-Bergmann, T., Riffel, R., et al. 2021b, MNRAS, 504, 3265, doi: 10.1093/mnras/stab998

—. 2023b, MNRAS, 521, 1832, doi: 10.1093/mnras/stad599

Rines, K. J., Geller, M. J., Diaferio, A., & Hwang, H. S. 2016, ApJ, 819, 63, doi: 10.3847/0004-637X/819/1/63

Ruschel-Dutra, D., Storchi-Bergmann, T., Schnorr-Müller, A., et al. 2021, MNRAS, 507, 74, doi: 10.1093/mnras/stab2058

Sakamoto, K., Aalto, S., Combes, F., Evans, A., & Peck, A. 2014, ApJ, 797, 90, doi: 10.1088/0004-637X/797/2/90

Sandage, A. 1966, ApJ, 145, 1, doi: 10.1086/148734

Smee, S. A., Gunn, J. E., Uomoto, A., et al. 2013, AJ, 146, 32, doi: 10.1088/0004-6256/146/2/32

Souza-Oliveira, G., Riffel, R., Costa-Souza, J. H., & Zakamska, N. 2024, ApJ, ??, ?/, doi: 10.1051/?

Stierwalt, S., Armus, L., Surace, J. A., et al. 2013, ApJS, 206, 1, doi: 10.1088/0067-0049/206/1/1

Storchi-Bergmann, T., McGregor, P. J., Riffel, R. A., et al. 2009, MNRAS, 394, 1148, doi: 10.1111/j.1365-2966.2009.14388.x

Thomas, D., Steele, O., Maraston, C., et al. 2013, MNRAS, 431, 1383, doi: 10.1093/mnras/stt261

Togi, A., & Smith, J. D. T. 2016, ApJ, 830, 18, doi: 10.3847/0004-637X/830/1/18

Tremblay, G. R., Chiaberge, M., Donzelli, C. J., et al. 2007, ApJ, 666, 109, doi: 10.1086/520333

Tully, R. B., & Pierce, M. J. 2000, ApJ, 533, 744, doi: 10.1086/308700

U, V., Lai, T., Bianchin, M., et al. 2022, ApJL, 940, L5, doi: 10.3847/2041-8213/ac961c

Véron-Cetty, M. P., & Véron, P. 2006, A&A, 455, 773, doi: 10.1051/0004-6361:20065177

Wells, M., Pel, J. W., Glasse, A., et al. 2015, PASP, 127, 646, doi: 10.1086/682281

Yuan, Y., & Neufeld, D. A. 2011, ApJ, 726, 76, doi: 10.1088/0004-637X/726/2/76

Zakamska, N. L. 2010, Nature, 465, 60, doi: 10.1038/nature09037